Biosensors and Bioelectronics 96 (2017) 89–98

Contents lists available at ScienceDirect

Biosensors and Bioelectronics

journal homepage: www.elsevier.com/locate/bios

Molecular overlap with optical near-fields based on plasmonic nanolithography for ultrasensitive label-free detection by light-matter colocalization

Kiheung Kim[a,1], Wonju Lee[a,1], Kyungwha Chung[b], Hongki Lee[a], Taehwang Son[a], Youngjin Oh[c], Yun-Feng Xiao[d], Dong Ha Kim[b], Donghyun Kim[a,*]

[a] School of Electrical and Electronic Engineering, Yonsei University, Seoul 03722, Republic of Korea
[b] Department of Chemistry and Nano Science, Ewha Womans University, Seoul 03760, Republic of Korea
[c] OLED Division, Samsung Display, Asan, Chungcheongnam-do 31454, Republic of Korea
[d] School of Physics, Peking University, Beijing 100871, PR China

ARTICLE INFO

Keywords:
Biosensor
Surface plasmon resonance
Plasmonic lithography
Sensitivity
Colocalization

ABSTRACT

In this work, we investigate the detection sensitivity of surface plasmon resonance (SPR) biosensors by engineering spatial distribution of electromagnetic near-fields for colocalization with molecular distribution. The light-matter colocalization was based on plasmonic nanolithography, the concept of which was confirmed by detecting streptavidin biotin interactions on triangular nanoaperture arrays after the structure of the aperture arrays was optimized for colocalization efficiency. The colocalization was shown to amplify optical signature significantly and thereby to achieve detection on the order of 100 streptavidin molecules with a binding capacity below 1 fg/mm^2, an enhancement by more than three orders of magnitude over conventional SPR detection.

1. Introduction

Numerous optical biosensing schemes have emerged for detecting molecular interactions. One of the most successful techniques has been the one based on surface plasmon resonance (SPR), which relies on the dependence of plasmon excitation on the changes of surface states as a result of biointeraction. In contrast to optical sensors that take advantage of labels such as fluorescent dyes and quantum dots, SPR detection measures refractive index change due to the change in mass bound to the sensor surface and is performed label-free, thus allows kinetics of target interactions to be measured without labeling interference in a quantitative manner and in real-time for a large range of analyte molecular weights (McDonnell, 2001). However, the label-free nature of SPR detection is accompanied by relatively moderate sensitivity as well. To achieve enhanced sensitivity, many strategies have been pursued, for example, by using molecular intermediaries such as nanoparticles and aptamers to amplify optical signatures (He et al., 2000; Moon et al., 2010; Bai et al., 2013). Also, phase detection has been conducted to measure phase changes caused by an interaction, rather than intensity (Nelson et al., 1996; Wu et al., 2004; Halpern et al., 2011). Binding area has been increased by surface corrugation which was often on a nanometer scale using nanowires or nanogrids (Kim et al., 2006; Byun et al., 2007b; Moon et al., 2012; Yu et al., 2013), while effects of surface curvature on the detection sensitivity were investigated (Lee and Kim, 2016). SPR detection has been combined with other sensing schemes that include magneto-optic modulation, microcavities and electron field-effects (Sepúlveda et al., 2006; Dantham et al., 2013; J. Oh et al., 2010). Of particular interest is colocalized detection between fields and target binding molecules that has been explored to improve sensitivity by spatially overlapping near-fields produced by 2D or 3D metallic surface nanostructures with target molecules (Shalabney and Abdulhalim, 2010; Lee and Kim, 2012), i.e., if a target molecule perturbs an ambient evanescent field, resonance shift δk may be represented as

$$\delta k \cong \frac{k_i}{2}\frac{\int_{V_P} \delta \in E_i^* E_f dr}{\int_V \in E_i^* E_t dr} \quad (1)$$

where k_i is the wave vector of incident light (Abdulhalim, 2007). The integral in the numerator is an overlap integral between distributions of binding molecules expressed as the difference in permittivity $\delta\varepsilon$ and light fields before (E_i) and after (E_f) the binding. The integral at the

* Corresponding author.
E-mail address: kimd@yonsei.ac.kr (D. Kim).
[1] These authors contributed equally to this work.

http://dx.doi.org/10.1016/j.bios.2017.04.046
Received 14 February 2017; Received in revised form 19 April 2017; Accepted 27 April 2017
Available online 28 April 2017

bottom is an energy integral that represents the total energy of the propagating mode and remains largely constant in the course of molecular interactions. Therefore, Eq. (1) suggests that sensitivity enhancement can be achieved as a result of efficient colocalization combined with near-field localization.

The colocalization has been implemented by oblique evaporation of mask layers or blocked copolymers so that the fields are maximally utilized for much enhanced detection (Ma et al., 2010; Y. Oh et al., 2010, 2014; Y. Kim et al., 2012; Jang et al., 2013). Colocalization is often performed by using colloidal plasmonic nanoparticles to localize target molecules specifically (Rong et al., 2008; Chaudhari and Pradeep, 2015) and graphene-based light confinement (Rodrigo et al., 2015). Effect of field overlap with an active layer was investigated thoroughly in plasmon detection on nanoporous medium (Berriera et al., 2011). Also, directed molecular binding was produced at nanogaps between metallic dimers (Aćimović et al., 2009; Feuz et al., 2012). The effectiveness of colocalization has not been limited to SPR detection and was in fact shown to be quite general, for example, in microcavity and waveguide sensors (Santiago-Cordoba et al., 2011; Dantham et al., 2012; Rodriguez et al., 2014; Shen et al., 2016), super-resolved imaging (K. Kim et al., 2012; W. Lee et al., 2015) and optical fiber sensors which maximize evanescent wave overlap with target analytes (Huntington et al., 1999; Kim et al., 2005; Martan et al., 2008). While colocalization approaches were shown both experimentally and theoretically to lead to enhanced detection sensitivity over conventional unlocalized SPR detection, the way that the colocalization is attained is oftentimes quite difficult and time-consuming, thus a more obvious and directed colocalization approach is highly desired.

In this paper, therefore, we explore use of plasmonic lithography to engineer electromagnetic wave distribution in the near-field to implement colocalized SPR detection that is more direct than traditional methods used for colocalization. In other words, detection area is defined by plasmonic lithography with a locally amplified light field (Fig. 1a) and then SPR detection is performed (Fig. 1b), the cross-section of which is shown in Fig. 1c. Plasmonic nanolithography has been developed as a technique that employs strongly amplified near-fields created by the excitation and transfer of surface plasmon (SP) for exposure in lithography (Srituravanich et al., 2004; Ozbay, 2006; El Ahrach et al., 2007; Ueno et al., 2010, 2011; Xie et al., 2011; Wirth et al., 2011). As a consequence, surface patterns formed by the development of photopolymers reflect the near-field distribution. Ideally, if SPR detection of an interaction is performed with a light source that is identical to the one used for the lithography, perfect colocalization can be easily achieved. Such a colocalization approach frees the need for surface-specific chemical modification that needs to be performed as a way to spatially localize an interaction and thus increases the versatility of colocalization-based sensitivity enhancement. In fact, SPR detection is often conducted at a longer wavelength for higher sensitivity (Nelson et al., 1999; Pang et al., 2007; Hotta et al., 2012), while exposure of photopolymers used in lithography requires high energy and thus short wavelength light source, thus giving rise to a disparity between patterning and measurement light wavelengths. Even if the patterning and measurement wavelengths were identical, the distribution of probe molecules that bind to target may still be different from that of near-fields: for example, probes distribute only on the surface whereas the near-field is in principle three-dimensional. In this sense, the disparity between molecular and field distribution may be inevitable to an extent. Therefore, we intend here to confirm the validity of the proposed colocalization based on plasmonic nanolithography and, more importantly, to assess the limit of detection (LOD) sensitivity under the scheme by investigating the wavelength disparity and its effect on the colocalized detection.

2. Methods and materials

2.1. Numerical calculation

The near-field distribution was produced by 3D nanoarrays as surface nanostructures for nanoplasmonic lithography and has been calculated using RCWA. RCWA has been used successfully to calculate optical characteristics of various nanostructures (Kanamori et al., 2001; Cesario et al., 2005; Byun et al., 2007a). The nanoarrays take a triangular shape for efficient near-field localization (Lee et al., 2012). For the calculation, 25×25 spatial harmonic orders were employed with *p*-polarized light incidence at each resonance angle, while the pattern size (L) was varied from 300 to 700 nm in a step of 100 nm at an array period (Λ) of 1 and 2 μm. Calculation was performed for both λ=442 and 633 nm. L refers to the side length of an equilateral triangle. The calculation was performed at a distance of z=10 nm from the nanoarray bottom as the molecular interaction takes place in this axial range. Once near-fields are calculated, colocalization efficiency η, which is defined as a normalized overlap signature between the fields produced at λ_1=442 nm and λ_2=633 nm, wavelength used respectively for light exposure and measurement, has been calculated numerically as an indirect measure of colocalization, i.e.,

$$\eta(\lambda_1, \lambda_2) = \frac{\int E_{t,\lambda 1}^2(\vec{r}) E_{t,\lambda 2}^2(\vec{r}) d\boldsymbol{r}}{\sqrt{\int [E_{t,\lambda 1}^2(\vec{r})]^2 d\boldsymbol{r} \int [E_{t,\lambda 2}^2(\vec{r})]^2 d\boldsymbol{r}}}. \quad (2)$$

Here, $E_{t,\lambda}$ represents normalized tangential electric field amplitude at a wavelength λ. Colocalization efficiency η defined in Eq. (2) in effect describes intensity correlation of electric field distribution at two different wavelengths (Adler and Parmryd, 2010).

Localized near-fields represent the amount of molecular probes in a probabilistic sense and have a quantitative importance on a relative scale. For this reason, we have calculated relative number of probes N_p which is defined as the normalized field intensity:

$$N_p(\lambda_2) = \int E_{t,\lambda 2}^2(\vec{r}) d\boldsymbol{r} / S_r. \quad (3)$$

In addition to η and N_p, we have also considered the resonance shift per unit molecule which we define as relative angle shift

$$RAS = \Delta\theta_{SPR}/S. \quad (4)$$

Here, $\Delta\theta_{SPR}$ represents the resonance angle shift as a result of an interaction. *RAS* is normalized by the surface area S which probe molecules can bind to and is thus proportionate to the amount of interaction (Oh et al., 2014; Korlach et al., 2008). Increased *RAS* can be attributed to more efficient overlap between field and target distribution.

2.2. Sample fabrication

Fabrication of samples consists mainly of three steps as illustrated in Fig. 2. First, electron-beam lithography was used to define nanoarrays. A 2-nm thick chrome adhesion layer, a 5-nm thick film of silver, and then a 1-nm chrome capping layer were evaporated on a cleaned SF10 glass substrate on which negative photoresist (AR.N 7520.18, Allresist™, Strausberg, Germany) was spin-coated at 4000 rpm and soft-baked on a hot plate at 85 °C. This was followed by e-beam exposure and development into a pattern on the PMMA layer. After secondary evaporation of silver in 50-nm thickness and removal of resist, an additional chrome capping layer of 1 nm was deposited to prevent instability of silver film while forming a metallic nanoarray pattern, which was then annealed at 80 °C for 30 mins (Wang et al., 2014). Nanolithography then ensues by spin-coating AR 3120 positive photoresist (Allresist™) at 8000 rpm. After baking the sample at 105 °C, light exposure was proceeded using a customized SPR set-up based on two concentric dual motorized stages and a laser diode (Model #: MDL-III-442, nominal power: 20 mW, λ=442 nm, Changchun Optoelectron. Technol. Corp., China), i.e., each nanoarray sample was exposed for 10 s under *p*-polarized light incident at θ_{in}=60°, while being index-matched to an SF10 prism substrate. Exposed photoresist was carefully developed by automating the process

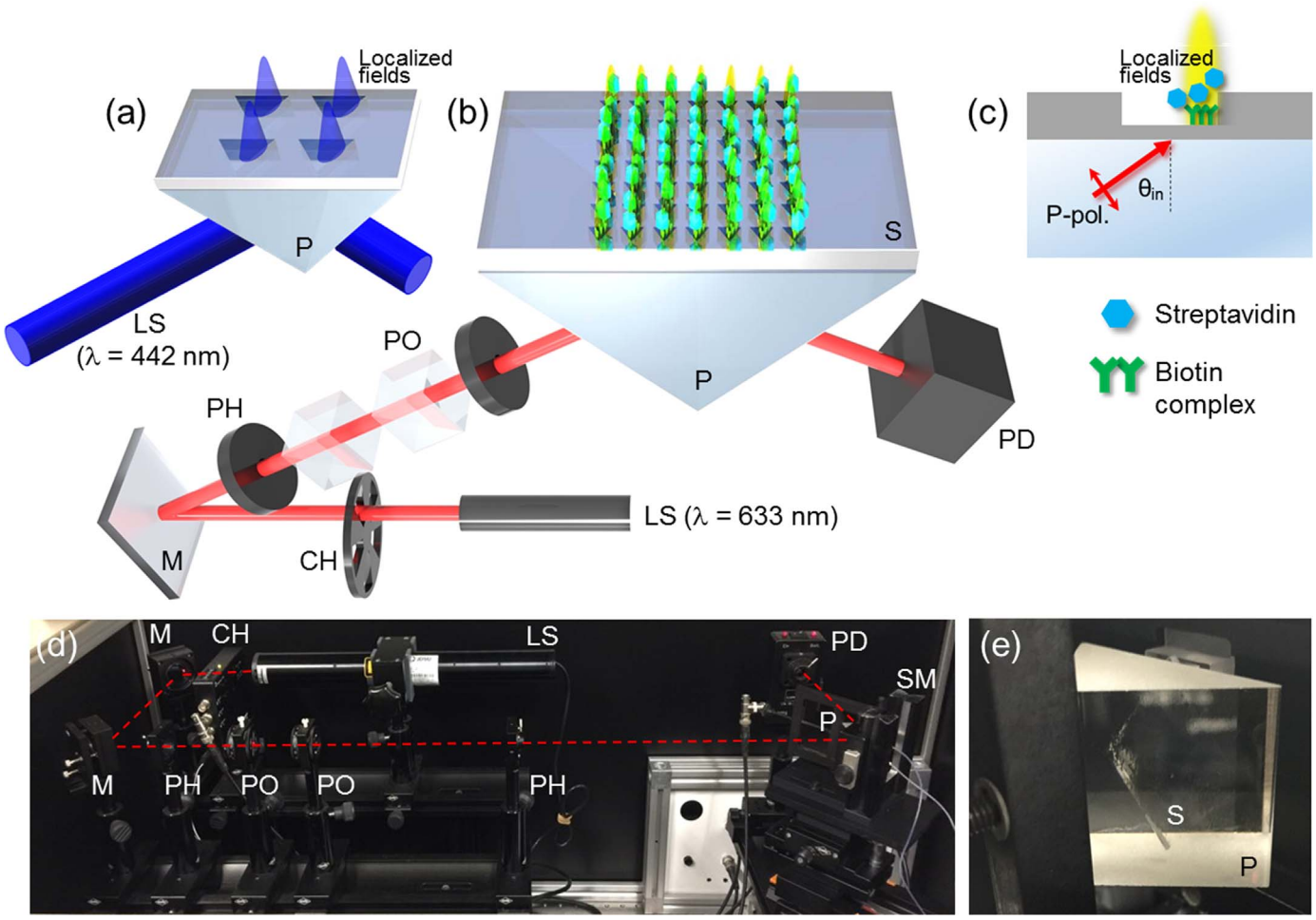

Fig. 1. Schematic illustration of plasmon nanolithography for colocalized SPR detection: (a) plasmonic lithography forms nanogaps at nanoaperture arrays, (b) SPR detection colocalizes near-fields with target-probe molecular binding, and (c) cross-sectional view of a nanogap. Photographs: (d) SPR measurement instrument set-up and (e) a nanogap array sample mounted on the prism for measurement (CH: chopper, LS: light source, M: mirror, PH: pinhole, PO: polarizers, SM: sample mount, S: sample, P: prism, and PD: photodetector). The dashed line in red represents interrogation light path. (For interpretation of the references to color in this figure legend, the reader is referred to the web version of this article).

for improved reproducibility. For control experiments, two different types of samples were prepared: first, a 50-nm thick film of silver without any patterns capped with 1-nm thick chrome on a SF10 glass substrate was fabricated. Second, PMMA grating pattern was formed after electron-beam lithography on the chrome/silver films deposited on an SF10 substrate. Both experiments intended to confirm the immobilization of probe molecules (biotin) and to check the influence of the removal process of resist by chemical remover (AR 300-70, Allresist™) on the probe immobilization.

2.3. Near-field scanning optical microscopy

Near-field distribution produced by fabricated nanoaperture samples was measured by a near-field scanning optical microscope (NSOM). Our NSOM is based on a commercial product (SNLG102NTF, NT-MDT, Moscow, Russia) using a tapered optical fiber probe (MONO450, LovaLite, Besançon, France) which has a metallized aperture of 70-nm diameter and coated with aluminum. The NSOM was modified to allow inclined light incidence on a total internal reflection fluorescence microscopy backbone (IX73, Olympus, Tokyo, Japan). Light source was provided by a wavelength-tunable ion laser system (35-LAP-431-230, CVI Melles Griot, California, USA) and its wavelength was tuned to 457 nm for plasmonic lithography. Considering the thickness of an SF10 substrate which is larger than the working distance (WD) of a usual high-NA objective lens, we have used a long-WD objective lens (LMPlanFLN50×, Olympus). With its NA of 0.5, near-field distribution was measured in an incident angular range of $\theta_m \leq 16.6°$.

2.4. Binding chemistry

For proof of principles, we have measured biotin/streptavidin interactions: nanoaperture samples were immersed in the biotinylated PEG-thiol (Biotin-PEG-SH) (2000 Da, Nanocs Inc., USA) aqueous solution (1 mM) for 24 h, then rinsed with deionized water and dried with nitrogen flow. Bio-repellant characteristic of PEG reduces non-specific binding that may exist other than specific biotin-streptavidin interactions (Prats-Alfonso et al., 2006; Jokerst et al., 2011).

After positioning biotin-PEG-SH-modified nanoaperture sample on the SPR spectrometer, streptavidin solution at varied concentrations (from *Streptomyces avidinii*, lyophilized from 10 mM potassium phosphate, Sigma-Aldrich) was injected for 30 min and then rinsed with 10 mM phosphate buffer saline (PBS, Sigma-Aldrich) solution. All the protocols were carried out under room temperature. A peristaltic pump (0.5 mL/min) was used to deliver streptavidin and PBS solutions. Samples were rinsed with PBS buffer for 10 min to eliminate non-specifically adsorbed streptavidin.

Control measurements were performed on a 50-nm thick gold thin film. Surface of gold thin film was treated with Biotin-PEG-SH (1 mM) for 24 h and rinsed with deionized water. Biotin-PEG-SH-modified Au thin film was positioned on the SPR spectrometer and following steps similar to those described above for nanoaperture samples were carried out.

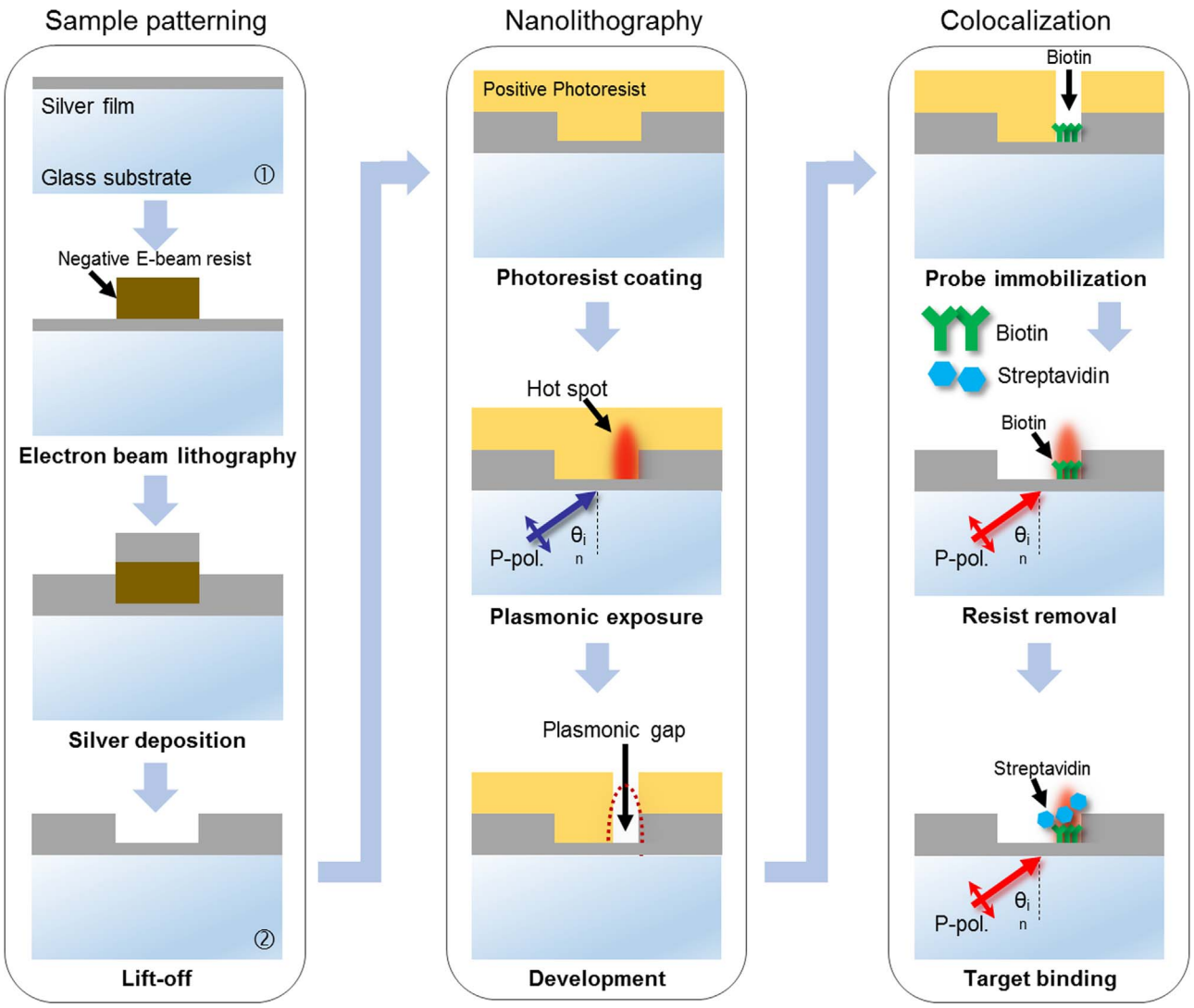

Fig. 2. Schematic illustration of fabrication steps of nanoarray patterns for colocalized SPR detection by plasmonic nanolithography The fabrication steps mainly consist of three steps: sample patterning, nanolithography, and colocalization. Control binding experiments of streptavidin-biotin interactions were conducted on thin film (①) and on nanoaperture arrays without colocalization (②).

2.5. SPR measurement

An SPR spectrometer (RT2005, Resonant Technologies GmbH, Germany) was used for SPR detection based on conventional θ–2θ architecture with a nominal angular resolution at 0.005°. For measurement, a sample was index-matched to an SF10 prism and illuminated by TM-polarized light from a He-Ne laser (λ=632.8 nm, 10 mW). Reflected light was measured by a silicon photodetector. Fig. 1b and c present the photographs of the set-up and a mounted sample for SPR measurement. The lowest detectable target concentration depends on various factors including target and probe molecular weight, probe surface coverage on the sensor surface, and the binding affinity of the target analyte molecules. The overall sensitivity of the SPR spectrometer in terms of binding capacity was estimated to be 10 pg/mm^2 (provided by the manufacturer). Because of the long pattern period (Λ=1 and 2 μm), higher diffraction orders may exist. For the range of experimental resonance angles, the higher-order diffraction is determined to be at least 13° away from the zeroth-order reflection by grating equation $\sin\theta_m = m\lambda/\Lambda + \sin\theta_{SPR}$ (m: an integer for the m-th order), thus the noise associated with higher-order diffraction can be easily removed from the photodiode.

3. Results and discussion

3.1. Control experiments

When we compare the immobilization of biotin and subsequent binding of streptavidin on a thin film surface without surface treatment by remover vs. binding after the treatment, the latter produced a much smaller resonance shift (Supporting information S1). Similar trends were observed with a grating pattern (Supporting information S2), i.e., resonance shift was smaller if binding takes place after removal of resist grating compared to the binding without removing the grating. These data suggest that the removal of resist should interfere with the immobilization. On the other hand, specific binding on the grating of polymer resist may be accompanied with nonspecific physisorption to polymer resist which can significantly affect the specific signal (Yu et al., 2012). For this reason, binding of streptavidin to biotin probe was performed after removal of photoresist, which was shown to reduce the surface density of probes significantly by 64% (Supporting information S2).

Nonspecific binding of streptavidin was also measured on PEGylated thin film surface. At a streptavidin concentration of

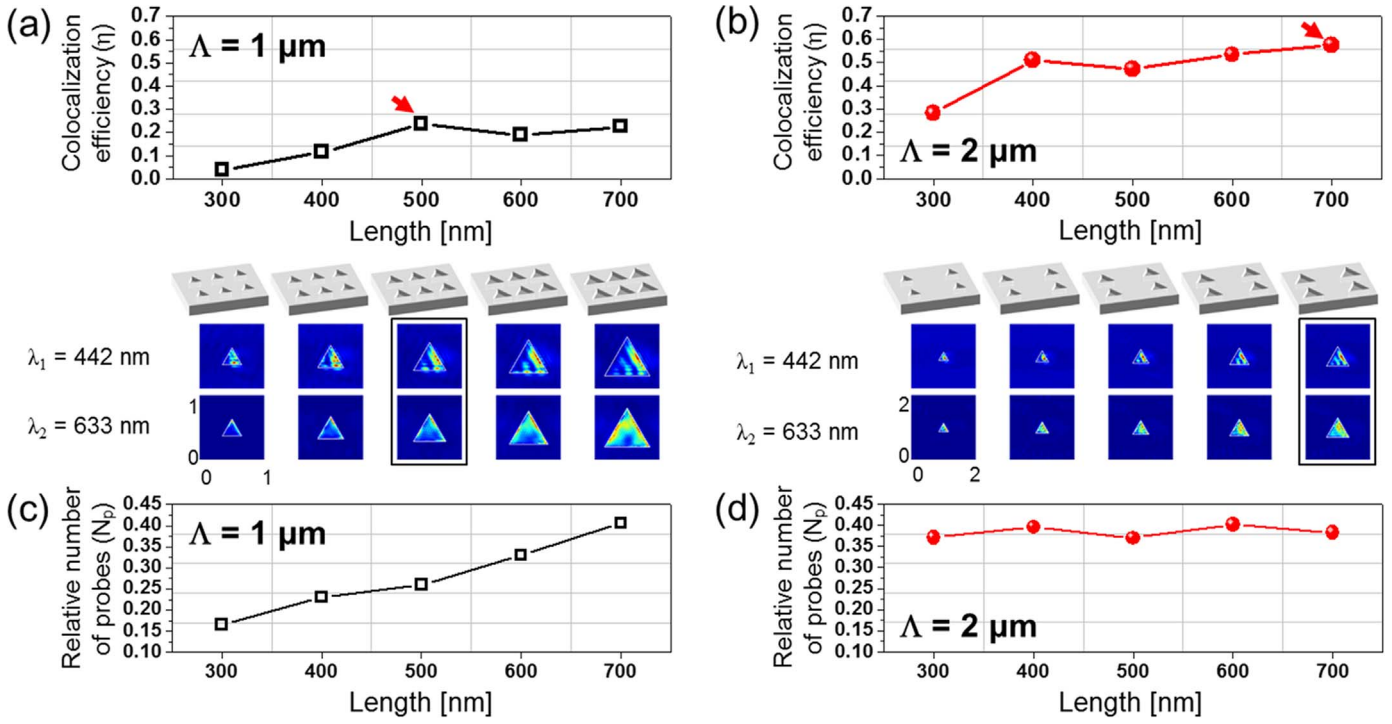

Fig. 3. Colocalization efficiency (η) for nanoarrays of the triangle side length L=300–700 nm: (a) Λ=1 μm and (b) 2 μm. Red arrows mark the highest colocalization efficiency at each period. In the middle are the near-field intensity distributions $|E|^2$ at λ_1=442 nm (upper row in each pair) and λ_2=633 nm (lower row). Relative number of probes (N_p) calculated at λ_2=633 nm as the array parameters are varied: (c) Λ=1 μm and (d) 2 μm. The calculation was performed for p-polarization (E-field in the xz plane) with the direction of light incidence horizontal from left to right in the top view. Each inset field distribution represents a unit area of (a,c) 1×1 μm^2 and (b,d) 2×2 μm^2. For all inset near-fields, $\theta_{in}=\theta_{SPR}$: in the boxed fields at L=500 nm and Λ=1 μm, θ_{in}=65.88° (λ_1=442 nm) and 56.75° (λ_2=633 nm). For the boxed fields at L=700 nm and Λ=2 μm, θ_{in}=66.81° (λ_1=442 nm), and 55.91° (λ_2=633 nm). (For interpretation of the references to color in this figure legend, the reader is referred to the web version of this article).

100 nM, $\Delta\theta_{SPR}$=0.053°. In order to compare detection characteristics such as sensitivity, control binding experiments of streptavidin-biotin interactions were conducted on thin film (① in Fig. 2) and on nanoaperture arrays without colocalization (②).

3.2. Nanoaperture design and near-fields

For the design of nanoarrays with high colocalization efficiency, colocalization efficiency η was calculated as the period (Λ) and the pattern size (L) were varied, at λ_1=442 nm and λ_2=633 nm, as shown in Fig. 3a and b. Also shown are the near-field distributions (top view in the xy plane) at λ_1=442 nm (upper row) and λ_2=633 nm (lower row) corresponding to the combinations of Λ and L in the inset. The near-field distribution was calculated for one unit (in an area of Λ^2) by rigorous coupled-wave analysis (RCWA) with periodic boundary conditions. The details of calculation are outlined in Methods and materials.

Overall, higher colocalization efficiency is observed at a longer period (Λ=2 μm) and also with a larger pattern size. This is due to the difficulty with which highly localized field at 442 nm that may form with shorter period and/or smaller size can be colocalized with the localized field at 633 nm. In the range of geometrical parameters that were simulated highest colocalization efficiency was 58%, which was obtained at Λ=2 μm and L=700 nm. For Λ=1 μm, highest colocalization efficiency was achieved to be 24% at L=500 nm. On the other hand, relative number of probe molecules N_p at λ_2=633 nm is presented in Fig. 3c and d. N_p represents the quantity proportionate to the nanoaperture area that may be produced by plasmonic lithography at λ_2=633 nm and to the amount of target-probe bindings. Therefore, the less localized the near-fields are, the higher N_p can be, as long as the fields remain strong enough for exposure in plasmonic lithography. Fig. 3c and d also suggest that pattern size should affect the degree of localization more than period does in the range of Λ=1–2 μm. Period shorter than 1 μm was not considered for ease of fabrication while at a longer period, localization may be reduced because of weakly coupling light fields.

The samples were fabricated following the details described in the methods section. Near-fields localized by the pattern at L=500 nm (Λ=1 μm) and L=700 nm (Λ=2 μm) are presented in the inset of Fig. 3c and d for λ_1=442 nm and λ_2=633 nm. The distribution shows a clear overlap of light at the two wavelengths, where the one at λ=442 nm represents the distribution of target-probe binding and the one at λ=633 nm that of localized field, thereby confirms the colocalization. A SEM image of a fabricated sample of triangular aperture arrays (L=700 nm and Λ=2 μm) is presented in Fig. 4a before plasmon lithography is performed. Fig. 4b shows near-field distribution measured by NSOM and overall confirms the strong localization along a triangular side opposite to the direction of light incidence, which is in good agreement with the results of the inset of Fig. 3d. Near-field intensity profiles measured over many periods of nanoapertures along the direction represented by the dashed line in Fig. 4b are shown in Fig. 4c. Clearly, the near-fields by which photoresist is to be exposed in plasmonic lithography are spatially repetitive with FWHM at 507 nm. Fig. 4d and e are AFM images of aperture patterns (L=700 nm and Λ=2 μm) transferred to polymer resist as a result of plasmon lithography before proceeding with streptavidin-biotin detection. The depth profile measured by AFM across the red dashed line in Fig. 4e is also presented and suggests that the surface area on which probe molecules may immobilize should be approximately on the order of 400×200 nm^2. When an exposed hole area is assumed to take an elliptical shape from AFM measurements of multiple nanoapertures, the effective area for colocalization S(colocalized) was determined slightly larger than Fig. 4e to be S(colocalized)=128,000 ± 38,900 nm^2 per unit square of Λ^2=4 μm^2 area.

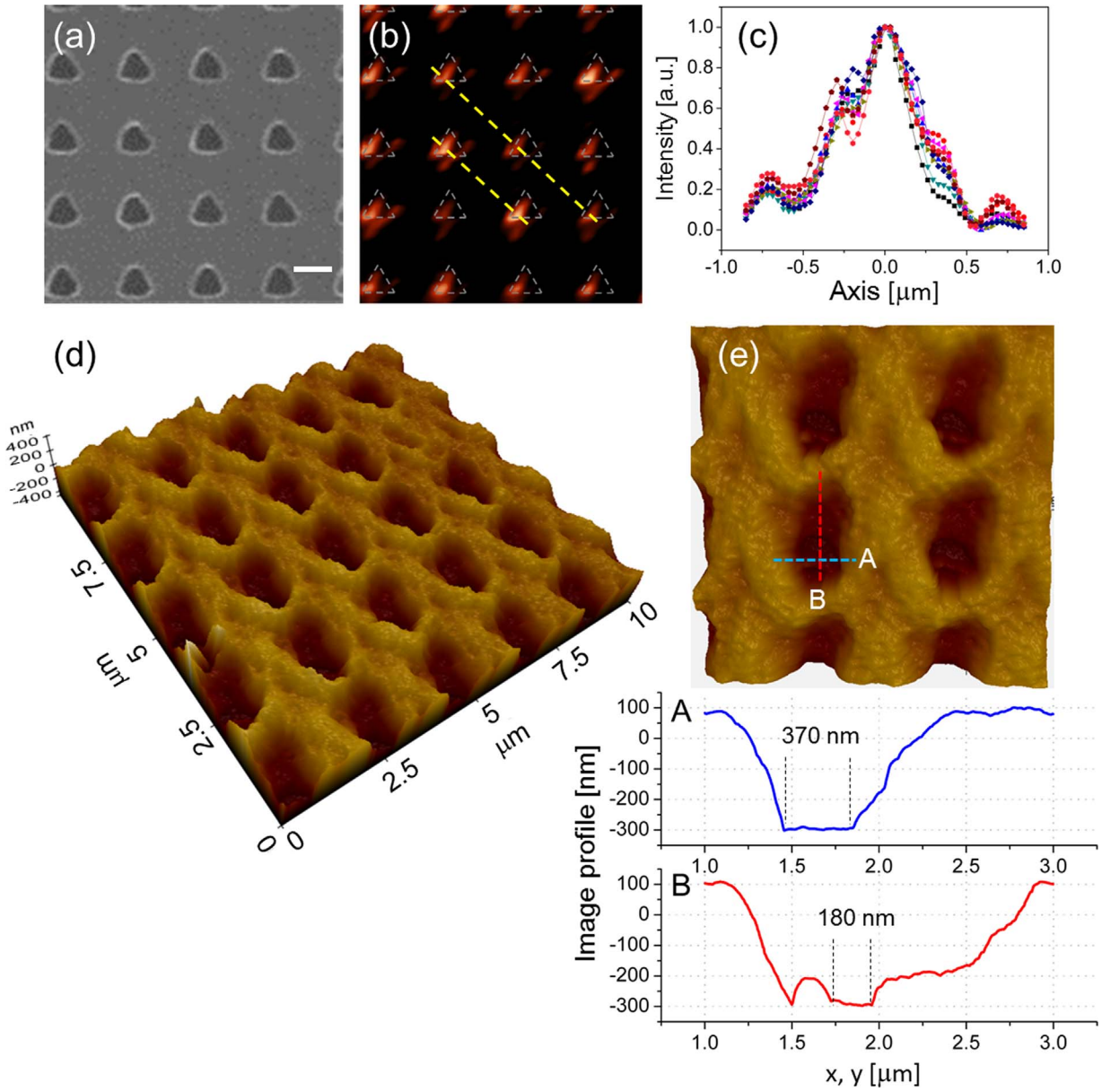

Fig. 4. (a) SEM image of a fabricated nanoarray sample with L=700 nm and Λ =2 μm after electron-beam lithography. (b) NSOM image of near-fields localized by nanoarrays (dashed triangles) for the sample in (a). Scale bars: 1 μm. (c) Intensity profiles of the measured near-fields across nine nanohole periods along the direction represented by the dashed line in (b). (d), (e) AFM images of a nanoarray sample on resist after plasmonic lithography. Depth profile measured by AFM across the horizontal (A) and vertical (B) dashed line in (e). The overall pattern depth is measured to be approx. 400 nm.

3.3. Colocalized detection

Fig. 5a shows the isotherm characteristics with streptavidin concentration, which was performed on metal thin films and nanoapertures arrays as control and sample experiments to confirm colocalized detection based on plasmonic lithography (angular spectra at 100 nM streptavidin concentration presented in Fig. 5b and c). For sample experiments, we have used nanoaperture arrays at L=700 nm (Λ=2 μm) per results that we obtained in the design process.

In both control and sample experiments, almost identical overall behavior is observed: with a high streptavidin concentration, the binding is limited by probe concentration. In this regime, optical response changes relatively little. A significant reduction of streptavidin concentration causes the binding to be governed by target concentration and the binding thus becomes target-limited. The transition between probe-limited and target-limited detection arises at a target concentration of around 50 nM. For very low streptavidin concentration, eventually noise prevails and gives rise to a noise floor that is due to the factors such as thermal and shot noise of the detector, stochastic nature of adsorption and desorption processes, and non-specific binding (Jakšić et al., 2014). The noise floor of the control measurement sets the detection limit to be on the order of 1 nM. The overall trend is in good agreement with the characteristics observed with our optical set-up for DNA hybridization (Oh et al., 2014).

It is clear that colocalized detection produces significantly larger optical signature than controls. In contrast, non-colocalized (or uncolocalized) detection improves the detection only marginally despite light localization, which is associated with an increased surface area: r_θ=$\Delta\theta_{SPR}$(colocalized)/$\Delta\theta_{SPR}$(thin film)=5.48 (=1.15/0.21) vs. $\Delta\theta_{SPR}$(non-colocalized)/$\Delta\theta_{SPR}$(thin film)=1.19 (=0.25/0.21) at target concentration of 100 nM. In addition, the rate of increase of resonance shifts is shown in Fig. 5d. Resonant shift measured by colocalized detection increases more markedly with target concentration than thin film controls by 1.72 (=0.4476/0.2605) times, while it is 1.37

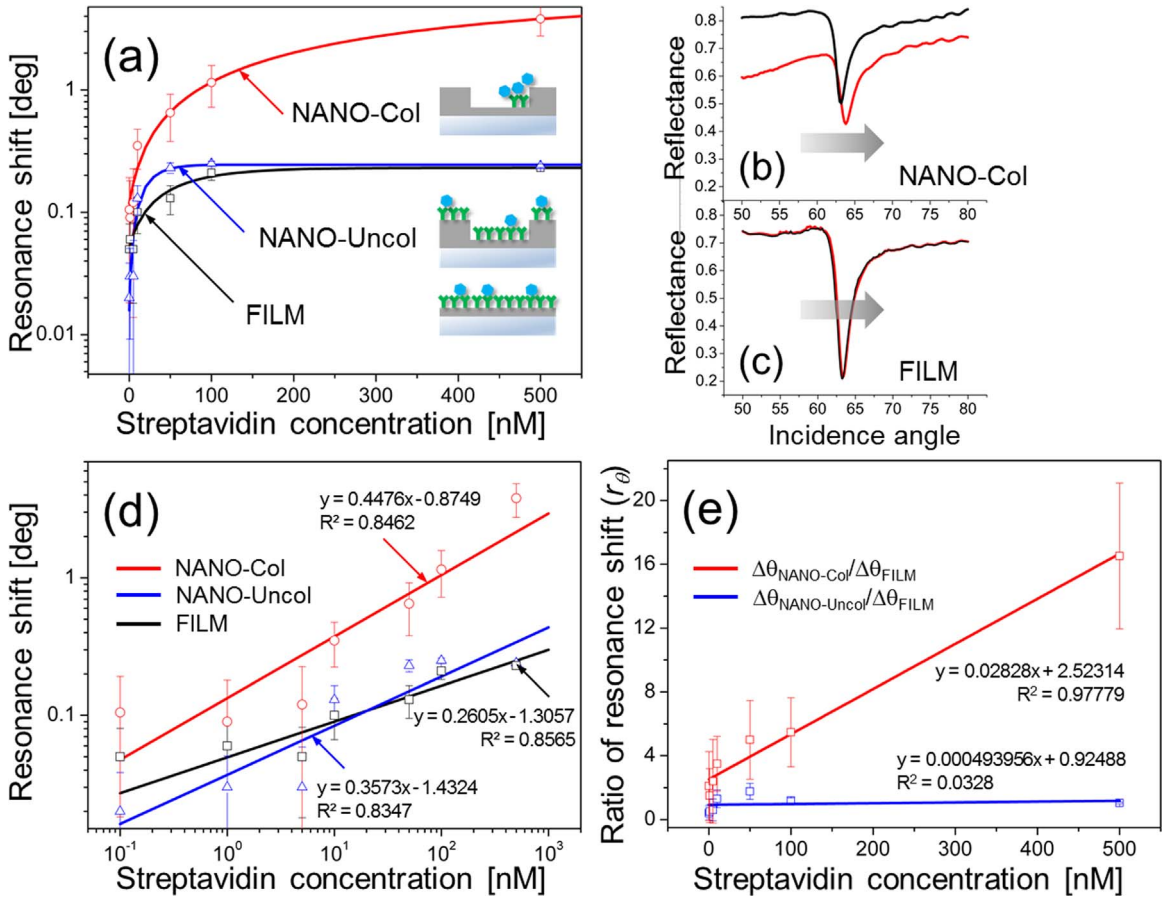

Fig. 5. Measured isotherm characteristics of streptavidin-biotin interactions: (a) resonance shift as the streptavidin target concentration is varied for control and colocalized detection with nanoapertures of L=700 nm and Λ=2 μm ('NANO-Col' and 'NANO-Uncol' for colocalized and non-colocalized detection and 'FILM' for control). Angular spectra represent characteristic changes in arrows as a result of the interaction at 100 nM streptavidin concentration: (b) colocalized (NANO-Col) and (c) control on film (FILM) before (black) and after (red) interactions. (d) Resonance shift with target concentration on a logarithmic scale. (e) Measured ratios of resonance shifts r_θ (NANO-Col/FILM vs. NANO-Uncol/FILM) with respect to target concentration. Results of linear regression are also shown. (For interpretation of the references to color in this figure legend, the reader is referred to the web version of this article).

(=0.3573/0.2605) times for non-colocalized detection. Note that r_θ increases almost linearly with target concentration, as shown in Fig. 5e, with a slope of 0.0278 ± 0.00223/nM (R^2=97.4%), i.e., colocalization produces much stronger optical signature at higher concentration compared to control measurement even with a smaller number of bound target molecules than the non-colocalized case, although relative standard deviation (RSD) tends to be larger (RSD=27.65% for colocalization and 4.93% for non-colocalization at a target concentration of 500 nM). Stronger enhancement of optical signature (r_θ) with target concentration appears to be related to the localization of SP for colocalized detection (Svedendahl et al., 2009). Also, measured resonance shift saturates at much higher target concentration than control measurements because an increase in target concentration in colocalized detection increases the resonance shift much more significantly, thus colocalized detection can be associated with a much wider dynamic range than non-colocalized case. To a weaker extent, steric hindrance of streptavidin in sample experiments may prevent more efficient binding to biotin molecules for both colocalized and non-colocalized detection.

We emphasize that a far smaller number of target-probe bindings are responsible for the increased signal of colocalized detection. The number of bindings may be proportionate to the area that is available for probes to bind, while the area as the number for colocalized detection can be underestimated due to the interference by the resist removal process as described in Supporting information S2. With an interference factor IF defined as the percentage amount of probes that is affected by the removal process, then the ratio of the effective areas is given by $r_s \equiv S$(thin film)/[(1−IF)·S(colocalized)], which is presumed not to significantly vary with target concentration, and the overall resonance enhancement $E \equiv RAS$(colocalized)/RAS(thin film)=$r_\theta \cdot r_s$. With IF=0.64 from Supporting information S2, r_s=86.8 ± 26.4 and measured resonance enhancement E=476 and 304 at target concentration of 100 and 10 nM, respectively. The results suggest that the enhancement should be mainly associated with reduced target-probe binding that is exposed to the localized field.

Note that Fig. 5a shows that rather than directly improving the detection limit, which is determined largely by the SPR measurement system, or reducing the minimum number of bindings that may be detectable, colocalization detection selectively amplifies the optical signature that is associated with or created by the unit binding event, thereby increases signal-to-noise ratio significantly. If we assume an incident beam of 650 μm in diameter, this encloses approximately 83,000 nanoapertures under measurement and the effective nanogap area in a beam spot available for immobilization of biotin as 10,600 ± 3200 μm^2. With surface coverage of biotin probes estimated at 3 molecules/nm^2 on thin gold films and 1−IF =36% as probe immobilization efficiency (Xia et al., 2012; Hinterwirth et al., 2013), the maximum number of biotin probes can be obtained as (1.1 ± 0.35)×10^{10} molecules.

Baseline data show that the blank standard deviation associated with non-specific adsorption is measured to be smaller than the angular resolution and therefore the LOD defined as the target concentration that is 3 times the standard deviation is much smaller than the noise floor presented in Fig. 5a and d for both colocalized

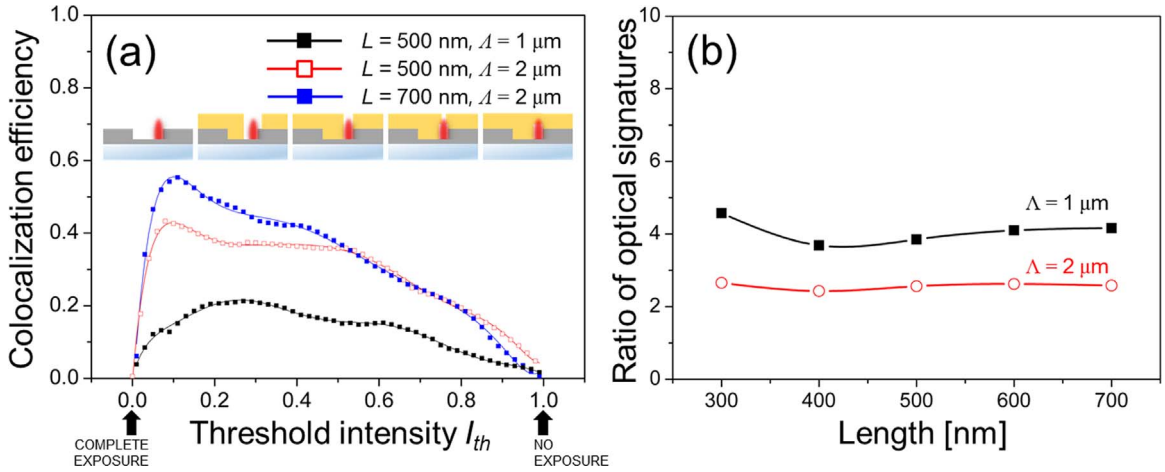

Fig. 6. (a) Colocalization efficiency for triangular nanoapertures with threshold exposure intensity I_{th}, which is defined as the field intensity normalized by the maximum when photoresist is presumed exposed if $|E|^2 \geq I_{th}$. Solid lines represent polynomial fits of calculated colocalization efficiency. (b) Ratio of optical signatures between target-probe interaction and non-specific adsorption. The ratio was calculated as $\sum \varepsilon E(\text{target-probe})^2 / \sum \varepsilon E(\text{non-specific})^2$ for various triangular nanoaperture arrays.

detection using nanoaperture arrays and control measurements (MacDougall and Crummett, 1980). Considering the effective number of binding events that participate in the colocalized detection is much smaller by r_s times than the case of non-colocalized detection, the effective LOD for colocalized detection amounts to be on the order of 30 pM (≈3 nM/86.8). This result confirms much improved LOD when compared to the past sensor data measuring streptavidin-biotin interactions based on microcavity (Vollmer et al., 2002) and plasmon resonance (Haes and Van Duyne, 2002; Riboh et al., 2003; Nusz et al., 2008; Kabashin et al., 2009). With a nominal and effective LOD of 10 nM and 30 pM, respectively, and molecular weight of streptavidin at 52.8 kDa, the detection sensitivity for colocalized detection (in terms of binding capacity) is then calculated to be well below 1 fg/mm^2 in an evanescent field that is 100 nm deep. In this range, a single molecule occupies an average area of about 9×9 μm^2 in the evanescent field and the number of target molecules under detection is projected to be on the order of 100 (see Supporting information S3 for details of calculation). Even after considering the uncertainty involved in the quantification under experimental environment, the detection in this range represents improvement by more than three-orders-of-magnitude, compared to conventional SPR detection (Campbell and Kim, 2007).

Interestingly, the results based on plasmonic nanolithography present higher enhancement compared to a previous study in which colocalized detection of 24-mer DNA hybridization was achieved by angled evaporation of a dielectric mask layer at triangular nanoaperture arrays at L=600 nm and Λ=2 μm (Oh et al., 2014). Herein, the evaporated dielectric mask often suffers from low uniformity and tends to form grains and random microstructures, which affects the distribution of localized fields and thus reduces colocalization efficiency. By comparison, the enhancement based on plasmonic nanolithography reported here appears to be substantially higher by at least 3 times. We believe that this result directly reflects the intuitive and intrinsic nature of plasmonic lithography for inducing field and matter colocalization.

3.4. Discussion

The significant resonance enhancement reported in this paper may be improved even further by addressing following issues that may prevent plasmonic lithography from achieving more efficient colocalization. First of all, the binary nature of exposure and development in plasmonic lithography may affect the resonance enhancement. While the distribution of localized light at λ=442 nm represents the likelihood of exposure at a particular location, the exposure is ultimately a binary process and the threshold light intensity above which photoresist is exposed and thereby developed cannot be ascertained on a quantitative basis. In other words, a developed pattern is not identical to the near-field distribution shown in the inset of Fig. 3c or d. Fig. 6a shows the colocalization efficiency η of selected triangular nanostructures as a function of threshold electric field intensity I_{th} when photoresist is presumed to be exposed for field intensity higher than the threshold, i.e., if $|E(x,y,z)|^2 \geq I_{th}$. Several observations are worth notes. First, regardless of I_{th}, optimum geometry largely remains unchanged, i.e., L=500 nm for Λ=1 μm and L=700 nm for Λ=2 μm. Higher colocalization efficiency at a longer period (Λ=2 μm) and a larger pattern size agree with what was observed in Fig. 3. It is also clear that colocalization is largely determined by the array period Λ and the effect of side length L is relatively weaker. Although it is difficult to precisely control I_{th}, an optimum I_{th} at which colocalization efficiency reaches at its highest is surprisingly low around 0.1 at Λ=2 μm and close to 0.3 at Λ=1 μm.

Enhancement may also come by reducing non-specific molecular signals and thus the LOD. Non-specific immobilization of biotin may be ignored due to the process described in Supporting information S1 and S2. On the other hand, non-specific physical adsorption of streptavidin on silver surface, even if the amount is insignificant, has its effect further weakened by the low field intensity of delocalized light fields. For quantitative assessment, optical signatures in terms of field-matter overlap εE^2 can be estimated: it is shown in Fig. 6b that the optical signature for target-probe interaction is at least 2.4 times stronger over non-specific adsorption for Λ=2 μm (higher as 3.6 times for Λ=1 μm), even in the worst case that the signal associated with non-specific adsorption is equal to what specific interaction may account for.

An obvious question to explore is the ultimate limit that may be achieved by colocalization. A simple numerical model using random nanoislands for field localization was established to show resonance enhancement by four orders of magnitude over non-specific detection of DNA hybridization (Yang et al., 2014). Even this, nor the results that we report here based on plasmonic lithography, does not appear to allow sensitivity sufficient for single molecule detection. One reason behind this is relatively inefficient light localization achieved by triangular nanoapertures. In principle, it is suggested that colocalization with more efficient super-localized light would lead to higher detection sensitivity: for example, light localization below 10 nm is known to be possible using gap-based aperture structures and/or pulsed light source (Fromm et al., 2004; H. Lee et al., 2015), potentially making it closer to molecular detection by SPR.

4. Concluding remarks

In summary, we have explored colocalized detection based on plasmonic nanolithography for maximizing spatial overlap between localized light fields and target molecular distribution. The concept was experimentally confirmed by detecting streptavidin-biotin interactions on triangular nanoaperture arrays. By overlapping the distribution of light fields and molecules in a conventional set-up, it was shown that light-matter colocalization can enhance detection sensitivity by more than three orders of magnitude over conventional thin-film based detection with achievable binding capacity below 1 fg/mm^2. The approach can be applied to improving detection characteristics such as signal-to-noise ratio in optical molecular measurement techniques.

Author statements

K. Kim fabricated samples and performed SPR experiments. W. Lee performed numerical calculation and set up plasmonic lithography. K. Chung performed chemistry and SPR experiments. H. Lee measured NSOM. T. Son helped set up plasmonic lithography. Y. Oh proposed the idea. Y.-F. Xiao discussed the results and helped analyze the data. D.H. Kim performed chemistry and measured SPR experiments. D. Kim wrote the manuscript and oversaw the work. Authors declare no competing financial interests in this study.

Acknowledgment

This work was supported by the National Research Foundation (NRF) Grants (NRF-2012R1A4A1029061, NRF-2015R1A2A1A100-52826,and NRF-2016K2A9A2A06004899). K. Chung and D.H. Kim acknowledge the financial support by the NRF of Korea Grant funded by the Korean Government (2014R1A2A1A09005656).

Appendix A. Supplementary material

Supplementary data associated with this article can be found in the online version at http://dx.doi.org/10.1016/j.bios.2017.04.046.

References

Abdulhalim, I., 2007. Biosensing configurations using guided wave resonant structures. In: Bock, W.J., Gannot, I., Tanev, S. (Eds.), Optical Waveguide Sensing and Imaging. Springer-Verlag, 211–228.

Aćimović, S.S., Kreuzer, M.P., González, M.U., Quidant, R., 2009. Plasmon near-field coupling in metal dimers as a step toward single-molecule sensing. ACS Nano 3, 1231–1237.

Adler, J., Parmryd, I., 2010. Quantifying colocalization by correlation: the Pearson correlation coefficient is superior to the Mander's overlap coefficient. Cytom. A 77A, 733–742.

Bai, Y., Feng, F., Zhao, L., Wang, C., Wang, H., Tian, M., Qin, J., Duan, Y., He, X., 2013. Aptamer/thrombin/aptamer-AuNPs sandwich enhanced surface plasmon resonance sensor for the detection of subnanomolar thrombin. Biosens. Bioelectron. 47, 265–270.

Berriera, A., Offermans, P., Cools, R., van Megen, B., Knoben, W., Vecchi, G., Rivas, J.G., Crego-Calama, M., Brongersma, S.H., 2011. Enhancing the gas sensitivity of surface plasmon resonance with a nanoporous silica matrix. Sens. Actuators B 160, 181–188.

Byun, K.M., Yoon, S.J., Kim, D., Kim, S.J., 2007a. Sensitivity analysis of a nanowire-based surface plasmon resonance biosensor in the presence of surface roughness. J. Opt. Soc. Am. A 24, 522–529.

Byun, K.M., Yoon, S.J., Kim, D., Kim, S.J., 2007b. Experimental study of sensitivity enhancement in surface plasmon resonance biosensors by use of periodic metallic nanowires. Opt. Lett. 32, 1902–1904.

Campbell, C.T., Kim, G., 2007. SPR microscopy and its applications to high-throughput analyses of biomolecular binding events and their kinetics. Biomaterials 28, 2380–2392.

Cesario, J., Quidant, R., Badenes, G., Enoch, S., 2005. Electromagnetic coupling between a metal nanoparticles grating and a metallic surface. Opt. Lett. 30, 3404–3406.

Chaudhari, K., Pradeep, T., 2015. In vitro colocalization of plasmonic nano-biolabels and biomolecules using plasmonic and Raman scattering microspectroscopy. J. Biomed. Opt. 20, 046011.

Dantham, V.R., Holler, S., Kolchenko, V., Wan, Z., Arnold, S., 2012. Taking whispering gallery-mode single virus detection and sizing to the limit. Appl. Phys. Lett. 101, 043704.

Dantham, V.R., Holler, S., Barbre, C., Keng, D., Kolchenko, V., Arnold, S., 2013. Label-free detection of single protein using a nanoplasmonic photonic hybrid microcavity. Nano Lett. 13, 3347–3351.

El Ahrach, H.I., Bachelot, R., Vial, A., Lérondel, G., Plain, J., Royer, P., Soppera, O., 2007. Spectral degeneracy breaking of the plasmon resonance of single metal nanoparticles by nanoscale near-field photopolymerization. Phys. Rev. Lett. 98, 107402.

Feuz, L., Jonsson, M.P., Höök, F., 2012. Material-selective surface chemistry for nanoplasmonic sensors: optimizing sensitivity and controlling binding to local hot spots. Nano Lett. 12, 873–879.

Fromm, D.P., Sundaramurthy, A., Schuck, P.J., Kino, G., Moerner, W.E., 2004. Gap-dependent optical coupling of single "Bowtie" nanoantennas resonant in the visible. Nano Lett. 4, 957–961.

Haes, A.J., Van Duyne, R.P., 2002. A nanoscale optical biosensor: sensitivity and selectivity of an approach based on the localized surface plasmon resonance spectroscopy of triangular silver nanoparticles. J. Am. Chem. Soc. 124, 10596–10604.

Halpern, A.R., Chen, Y., Corn, R.M., Kim, D., 2011. Surface plasmon resonance phase imaging measurements of patterned monolayers and DNA adsorption onto microarrays. Anal. Chem. 83, 2801–2806.

He, L., Musick, M.D., Nicewarner, S.R., Salinas, F.G., Benkovic, S.J., Natan, M.J., Keating, C.D., 2000. Colloidal Au enhanced surface plasmon resonance for ultrasensitive detection of DNA hybridization. J. Am. Chem. Soc. 122, 9071–9077.

Hinterwirth, H., Kappel, S., Waitz, T., Prohaska, T., Lindner, W., Lämmerhofer, M., 2013. Quantifying thiol ligand density of self-assembled monolayers on gold nanoparticles by inductively coupled plasma-mass spectrometry. ACS Nano 7, 1129–1136.

Hotta, K., Yamaguchi, A., Teramae, N., 2012. Nanoporous waveguide sensor with optimized nanoarchitectures for highly sensitive label-free biosensing. ACS Nano 6, 1541–1547.

Huntington, S.T., Katsifolis, J., Moar, P.N., Mulvaney, P., Roberts, A., Cahill, L.W., Nugent, K.A., 1999. Evanescent field characterisation of tapered optical fbre sensors in liquid environments using near feld scanning optical microscopy and atomic force microscopy. In: Proceedings of the IEEE Optoelectronics, IET. Vol. 146, pp 239–243.

Jakšić, O.M., Jakšić, Z.S., Čupić, Ž.D., Randjelović, D.V., Kolar-Anić, L.Z., 2014. Fluctuations in transient response of adsorption-based plasmonic sensors. Sens. Actuators B 190, 419–428.

Jang, Y.H., Chung, K., Quan, L.N., Spackova, B., Sipova, H., Moon, S., Cho, W.J., Shin, H.Y., Jang, Y.J., Lee, J.E., Kochuveedu, S.T., Yoon, M.J., Kim, J., Yoon, S., Kim, J.K., Kim, D., Homola, J., Kim, D.H., 2013. Configuration-controlled Au nanocluster arrays on inverse micelle nano-patterns: versatile platforms for SERS and SPR sensors. Nanoscale 5, 12261–12271.

Jokerst, J.V., Lobovkina, T., Zare, R.N., Gambhir, S.S., 2011. Nanoparticle PEGylation for imaging and therapy. Nanomedicine 6, 715–728.

Kabashin, A.V., Evans, P., Pastkovsky, S., Hendren, W., Wurtz, G.A., Atkinson, R., Pollard, R., Podolskiy, V.A., Zayats, A.V., 2009. Plasmonic nanorod metamaterials for biosensing. Nat. Mater. 8, 867–871.

Kanamori, Y., Hane, K., Sai, H., Yugami, H., 2001. 100 nm period silicon antireflection structures fabricated using a porous alumina membrane mask. Appl. Phys. Lett. 78, 142–143.

Kim, K., Yoon, S.J., Kim, D., 2006. Nanowire-based enhancement of localized surface plasmon resonance for highly sensitive detection: a theoretical study. Opt. Express 14, 12419–12431.

Kim, K., Yajima, J., Oh, Y., Lee, W., Oowada, S., Nishizaka, T., Kim, D., 2012b. Nanoscale localization sampling based on nanoantenna arrays for super-resolution imaging of fluorescent monomers on sliding microtubules. Small 8, 892–900.

Kim, Y., Chung, K., Lee, W., Kim, D.H., Kim, D., 2012a. Nanogap-based dielectric-specific colocalization for highly sensitive surface plasmon resonance detection of biotin-streptavidin interactions. Appl. Phys. Lett. 101, 233701.

Kim, Y.-C., Peng, W., Banerji, S., Booksh, K.S., 2005. Tapered fiber optic surface plasmon resonance sensor for analyses of vapor and liquid phases. Opt. Lett 30, 2218–2220.

Korlach, J., Marks, P.J., Cicero, R.L., Gray, J.J., Murphy, D.L., Roitman, D.B., Pham, T.T., Otto, G.A., Foquet, M., Turner, S.W., 2008. Selective aluminum passivation for targeted immobilization of single DNA polymerase molecules in zero-mode waveguide nanostructures. Proc. Natl. Acad. Sci. USA 105, 1176–1181.

Lee, H., Kim, D., 2016. Curvature effects on flexible surface plasmon resonance biosensing: segmented-wave analysis. Opt. Express 24, 11994–12006.

Lee, H., Kim, C., Kim, D., 2015. Sub-10 nm near-field localization by plasmonic metal nanoaperture arrays with ultrashort light pulses. Sci. Rep. 5, 17584.

Lee, W., Kim, D., 2012. Field-matter integral overlap to estimate the sensitivity of surface plasmon resonance biosensors. J. Opt. Soc. Am. A 29, 1367–1376.

Lee, W., Kim, K., Kim, D., 2012. Electromagnetic near-field nanoantennas for subdiffraction-limited surface plasmon-enhanced light microscopy. IEEE J. Sel. Top. Quantum Electron. 18, 1684–1691.

Lee, W., Kinosita, Y., Oh, Y., Mikami, N., Yang, H., Miyata, M., Nishizaka, T., Kim, D., 2015b. Three-dimensional superlocalization imaging of gliding mycoplasma mobile by extraordinary light transmission through arrayed nanoholes. ACS Nano 9, 10896–10908.

Ma, K., Kim, D.J., Kim, K., Moon, S., Kim, D., 2010. Target-localized nanograting-based surface plasmon resonance detection toward label-free molecular biosensing. IEEE J. Sel. Top. Quantum Electron. 16, 1004–1014.

MacDougall, D., Crummett, W.B., 1980. Guidelines for data acquisition and data quality evaluation in environmental chemistry. Anal. Chem. 52, 2242–2249.

Martan, T., Kanka, J., Kasik, I., Matejec, V., 2008. Tapered optical fibres for sensing. In:

Proceedings of the Photonics, Devices and Systems IV, SPIE. Vol. 7138.
McDonnell, J.D., 2001. Surface plasmon resonance: towards an understanding of the mechanisms of biological molecular recognition. Curr. Opin. Chem. Biol. 5, 572–577.
Moon, S., Kim, D.J., Kim, K., Kim, D., Lee, H., Lee, K., Haam, S., 2010. Surface-enhanced plasmon resonance detection of nanoparticle-conjugated DNA hybridization. Appl. Opt. 49, 484–491.
Moon, S., Kim, Y., Oh, Y., Lee, H., Kim, H.C., Lee, K., Kim, D., 2012. Grating-based surface plasmon resonance detection of core-shell nanoparticle mediated DNA hybridization. Biosens. Bioelectron. 32, 141–147.
Nelson, B.P., Frutos, A.G., Brockman, J.M., Corn, R.M., 1999. Near-infrared surface plasmon resonance measurements of ultrathin films. 1. Angle shift and SPR imaging experiments. Anal. Chem. 71, 3928–3934.
Nelson, S.G., Johnston, K.S., Yee, S.S., 1996. High sensitivity surface plasmon resonance sensor based on phase detection. Sens. Actuators B 35, 187–191.
Nusz, G.J., Marinakos, S.M., Curry, A.C., Dahlin, A., Höök, F., Wax, A., Chilkoti, A., 2008. Label-free plasmonic detection of biomolecular binding by a single gold nanorod. Anal. Chem. 80, 984–989.
Oh, J., Chang, Y.W., Yoo, S., Kim, D.J., Im, S., Park, Y.J., Kim, D., Yoo, K.-H., 2010a. Carbon nanotube-based dual mode biosensor for electrical and surface plasmon resonance measurements. Nano Lett. 10, 2755–2760.
Oh, Y., Lee, W., Kim, D., 2010b. Colocalization of gold nanoparticle-conjugated DNA hybridization for enhanced surface plasmon detection using nanograting antennas. Opt. Lett. 36, 1353–1355.
Oh, Y., Lee, W., Kim, Y., Kim, D., 2014. Self-aligned colocalization of 3D plasmonic nanogap arrays for ultra-sensitive surface plasmon resonance detection. Biosens. Bioelectron. 51, 401–407.
Ozbay, E., 2006. Plasmonics: merging photonics and electronics at nanoscale dimensions. Science 311, 189–193.
Pang, L., Hwang, G.M., Slutsky, B., Fainman, Y., 2007. Spectral sensitivity of two-dimensional nanohole array surface plasmon polariton resonance sensor. Appl. Phys. Lett. 91, 123112.
Prats-Alfonso, E., García-Martín, F., Bayo, N., Cruz, L.J., Pla-Roca, M., Samitier, J., Errachidb, A., Albericio, F., 2006. Facile solid-phase synthesis of biotinylated alkyl thiols. Tetrahedron 62, 6876–6881.
Riboh, J.C., Haes, A.J., McFarland, A.D., Yonzon, C.R., Van Duyne, R.P., 2003. A nanoscale optical biosensor: real-time immunoassay in physiological buffer enabled by improved nanoparticle adhesion. J. Phys. Chem. B 107, 1772–1780.
Rodrigo, D., Limaj, O., Janner, D., Etezadi, D., de Abajo, F.J.G., Pruneri, V., Altug, H., 2015. Mid-infrared plasmonic biosensing with graphene. Science 349, 165–168.
Rodriguez, G.A., Ryckman, J.D., Jiao, Y., Weiss, S.M., 2014. A size selective porous silicon grating-coupled Bloch surface and sub-surface wave biosensor. Biosens. Bioelectron. 53, 486–493.
Rong, G., Wang, H., Skewis, L.R., Reinhard, B.M., 2008. Resolving sub-diffraction limit encounters in nanoparticle tracking using live cell plasmon coupling microscopy. Nano Lett. 8, 3386–3393.
Santiago-Cordoba, M.A., Boriskina, S.V., Vollmer, F., Demirel, M.C., 2011. Nanoparticle-based protein detection by optical shift of a resonant microcavity. Appl. Phys. Lett. 99, 073701.
Sepúlveda, B., Calle, A., Lechuga, L.M., Armelles, G., 2006. Highly sensitive detection of biomolecules with the magneto-optic surface-plasmon-resonance sensor. Opt. Lett. 31, 1085–1087.
Shalabney, A., Abdulhalim, I., 2010. Electromagnetic fields distribution in multilayer thin film structures and the origin of sensitivity enhancement in surface plasmon resonance sensors. Sens. Actuators A 159, 24–32.
Shen, B.-Q., Yu, X.-C., Zhi, Y., Wang, L., Kim, D., Gong, Q., Xiao, Y.-F., 2016. Detection of single nanoparticles using the dissipative interaction in a high-Q microcavity. Phys. Rev. Appl. 5, 024011.
Srituravanich, W., Fang, N., Sun, C., Luo, Q., Zhang, X., 2004. Plasmonic nanolithography. Nano Lett. 4, 1085–1088.
Svedendahl, M., Chen, S., Dmitriev, A., Käll, M., 2009. Refractometric sensing using propagating versus localized surface plasmons: a direct comparison. Nano Lett. 9, 4428–4433.
Ueno, K., Takabatake, S., Nishijima, Y., Mizeikis, V., Yokota, Y., Misawa, H., 2010. Nanogap-assisted surface plasmon nanolithography. J. Phys. Chem. Lett. 1, 657–662.
Ueno, K., Takabatake, S., Onishi, K., Itoh, H., Nishijima, Y., Misawa, H., 2011. Homogeneous nano-patterning using plasmon-assisted photolithography. Appl. Phys. Lett. 99, 011107.
Vollmer, F., Braun, D., Libchaber, A., Khoshsima, M., Teraoka, I., Arnold, S., 2002. Protein detection by optical shift of a resonant microcavity. Appl. Phys. Lett. 80, 4057.
Wang, Z., Cheng, Z., Singh, V., Zheng, Z., Wang, Y., Li, S., Song, L., Zhu, J., 2014. Stable and sensitive silver surface plasmon resonance imaging sensor using trilayered metallic structures. Anal. Chem. 86, 1430–1436.
Wirth, J., Garwe, F., Hähnel, G., Csáki, A., Jahr, N., Stranik, O., Paa, W., Fritzsche, W., 2011. Plasmonic nanofabrication by long-range excitation transfer via DNA nanowire. Nano Lett. 11, 1505–1511.
Wu, S.Y., Ho, H.P., Law, W.C., Lin, C., Kong, S.K., 2004. Highly sensitive differential phase-sensitive surface plasmon resonance biosensor based on the Mach-Zehnder configuration. Opt. Lett. 29, 2378–2380.
Xia, X., Yang, M., Wang, Y., Zheng, Y., Li, Q., Chen, J., Xia, Y., 2012. Quantifying the coverage density of poly(ethylene glycol) chains on the surface of gold nanostructures. ACS Nano 6, 512–522.
Xie, Z., Yu, W., Wang, T., Zhang, H., Fu, Y., Liu, H., Li, F., Lu, Z., Sun, Q., 2011. Plasmonic nanolithography: a review. Plasmon 6, 565–580.
Yang, H., Lee, W., Hwang, T., Kim, D., 2014. Probabilistic evaluation of surface-enhanced localized surface plasmon resonance biosensing. Opt. Express 22, 28412–28426.
Yu, H., Oh, Y., Kim, S., Song, S.H., Kim, D., 2012. Polarization extinction-based detection of DNA hybridization in situ using a nanoparticle wire-grid polarizer. Opt. Lett. 37, 3867–3869.
Yu, H., Kim, K., Ma, K., Lee, W., Choi, J.-W., Yun, C.-O., Kim, D., 2013. Enhanced detection of virus particles by nanoisland-based localized surface plasmon resonance. Biosens. Bioelectron. 41, 249–255.